
GEOMETRY-AWARE PHYSICS-INFORMED POINTNETS FOR MODELING FLOWS ACROSS POROUS STRUCTURES

A PREPRINT

 Luigi Ciceri

Università degli Studi di Milano-Bicocca
Milan, Italy
l.ciceri7@campus.unimib.it

 Corrado Mio

Khalifa University of Science and Technology
Abu Dhabi, UAE
corrado.mio@ku.ac.ae

 Jianyi Lin

Università Cattolica del Sacro Cuore
Milan, Italy
jianyi.lin@unicatt.it

 Gabriele Gianini

Università degli Studi di Milano-Bicocca
Milan, Italy
gabriele.gianini@unimib.it

February 17, 2026

ABSTRACT

Predicting flows that occur both through and around porous bodies is challenging due to coupled physics across fluid and porous regions and the need to generalize across diverse geometries and boundary conditions. We address this problem using two Physics Informed learning approaches: Physics Informed PointNets (PIPN) and Physics Informed Geometry Aware Neural Operator (PI-GANO). We enforce the incompressible Navier Stokes equations in the free-flow region and a Darcy Forchheimer extension in the porous region within a unified loss and condition the networks on geometry and material parameters. Datasets are generated with OpenFOAM on 2D ducts containing porous obstacles and on 3D windbreak scenarios with tree canopies and buildings. We first verify the pipeline via the method of manufactured solutions, then assess generalization to unseen shapes, and for PI-GANO, to variable boundary conditions and parameter settings. The results show consistently low velocity and pressure errors in both seen and unseen cases, with accurate reproduction of the wake structures. Performance degrades primarily near sharp interfaces and in regions with large gradients. Overall, the study provides a first systematic evaluation of PIPN/PI-GANO for simultaneous through-and-around porous flows and shows their potential to accelerate design studies without retraining per geometry.

Keywords Physics-Informed Neural Networks (PINN); PointNets; Physics-Informed Geometry-Aware Neural Operator (PIGANO); Navier–Stokes equation; Porous media flows; Darcy law; Forchheimer equation; Penalization method; Computational Fluid Dynamics; Irregular geometries.

1 Introduction

Flows that occur through and around porous bodies at different scales are central to applications such as submerged breakwaters, rock-filled gabions, industrial filters, catalytic beds, heat exchangers, and even biological systems such as coral reefs or plant canopies. Another notable application are windbreaks [1], such as vegetation barriers, fences, and perforated facades of buildings, used in various environmental and wind mitigation applications. In these cases, accurate prediction is essential because the interplay between the internal flow through the porous structure and the external flow around it controls transport efficiency, drag forces, and overall system performance.

Modeling such scenarios is doubly complex: the flow through the porous matrix depends on microstructural properties like porosity and permeability, while the flow around the body is influenced by external geometry and boundary layer dynamics. The problem is normally addressed using Computational Fluid Dynamics (CFD) [2, 3, 4, 5, 6, 7, 8], by solving the governing Navier-Stokes fluid equations [9] (and their extensions) to different regions of a discretized spatial domain (e.g., the Darcy-Forchheimer model for the porous region [10]). Capturing both regimes simultaneously in CFD requires fine spatial resolution and coupled modeling, leading to a high computational cost. An additional challenge is given by the need to generalize to different geometries: this is necessary for design and optimization workflows, where one must rapidly evaluate many shape variants without rerunning full-scale simulations for each case.

The first two challenges can be addressed using machine learning approaches recently introduced for fluid flow prediction, which, however, have not yet been applied to the simultaneous modeling of flows both through and around porous bodies. Physics-Informed Neural Networks (PINNs) [11] embed the governing equations of fluid flow directly into the training loss, allowing models to learn solutions that satisfy physical laws even when data are sparse. To address the geometry generalization challenge one can resort to a kind of "geometry-informed" networks, the PointNet [12]: these are neural architectures designed to process unstructured point cloud data, which makes them well suited for representing complex geometries without requiring a regular grid.

Physics-Informed PointNets [13] (PIPNet) combine the capabilities of PINNs and PointNets. Furthermore, based on PIPNet, the Physics-Informed Geometry-Aware Neural Operator (PI-GANO) [14] extends the paradigm by learning mappings between geometric configurations and solution fields *in operator form*, allowing for even greater generalization across boundary conditions. The PI-GANO approach, by further adapting the model to incorporate the parameters of the equations, can also predict solutions for previously unseen parameter values, opening opportunities for engineering applications.

A first contribution of the present study consists in addressing, for the first time, the challenge of predicting steady incompressible flows both through and around porous bodies of arbitrary geometries based on the the Navier-Stokes and Darcy-Forchheimer equations by leveraging the PIPNet and PI-GANO architectures, i.e. without retraining for each geometry.

The second contribution consists in extending both the PI-GANO architecture to handle 3D cases which are notoriously expensive to simulate using classic solvers. Moreover the conducted experiments included extremely complex and irregular geometries, such as trees and houses, allowing to test the true capabilities of the architecture in almost real world scenarios.

The experimentation is conducted on CFD-simulated datasets generated with OpenFOAM [15], an open-source computational fluid dynamics toolbox, using stylized porous body and shape configurations. The emphasis of this work is on addressing the computational challenges inherent in this double-flow regime and assessing the performance of different architectures, rather than on the detailed physical modeling of the porous microstructure.

The remainder of this paper is organized as follows. Section 2 introduces the governing equations for steady incompressible flow in porous media and describes the range of geometries considered. The simulation setup, data set generation, and point-cloud conversion are then presented. Section 4 details the Physics-Informed PointNet and PI-GANO methodologies, including the formulation of the physics-informed loss and the network architectures. Section 5 reports the results for 2D and 3D porous flow predictions, and for tests of generalization to unseen geometries. Finally, Section 6 summarizes the main findings and discusses directions for future work.

The source code [16] is publicly available.

2 Fluid Motion Equations and Problem Setup

We consider a domain consisting of a porous region Ω_p embedded in a free-fluid region Ω_f , with interface $\partial\Omega_p$ and outer boundary $\partial\Omega_f$ (cf. [3]). The governing PDEs can be expressed as $\mathcal{N}_{\Omega_p}[u(x), \lambda, \phi(x)] = 0$, $x \in \Omega_p$, and $\mathcal{N}_{\Omega_f}[u(x), \lambda] = 0$, $x \in \Omega_f$, subject to boundary conditions $\mathcal{B}_{\partial\Omega_p}[u(x)] = g(x)$ and $\mathcal{B}_{\partial\Omega_f}[u(x)] = h(x)$. On $\partial\Omega_p$, velocity and stress continuity are imposed; on $\partial\Omega_f$, standard inflow, outflow and wall conditions are applied. Our goal is to find $u(x)$ satisfying both PDEs, while parameterizing the neural models with respect to geometry $\partial\Omega_p$ and porosity $\phi(x)$ to test generalization to unseen systems.

2.1 Navier-Stokes and Darcy-Forchheimer Models

Consider a fluid described by the incompressible, steady Navier-Stokes equations:

$$\nabla \cdot \mathbf{u} = 0 \quad (1)$$

$$\rho(\mathbf{u} \cdot \nabla) \mathbf{u} = -\nabla p + \mu \nabla^2 \mathbf{u}, \quad (2)$$

valid in the free-fluid region Ω_f . Here \mathbf{u} is the velocity, p the pressure, ρ the density and μ the dynamic viscosity.

In the porous region Ω_p , additional drag terms are introduced to represent resistance of the solid matrix. The Darcy–Forchheimer form of Eq. 2 reads

$$\rho(\mathbf{u} \cdot \nabla) \mathbf{u} = -\nabla p + \mu \nabla^2 \mathbf{u} - \left(\mu D + \frac{1}{2} \rho F |\mathbf{u}| \right) \mathbf{u}, \quad (3)$$

with D the Darcy and F the Forchheimer coefficients. The linear term $\mu D \mathbf{u}$ models viscous drag, while the quadratic term accounts for inertial corrections at moderate pore scale Reynolds numbers [17]. For packed spheres these coefficients can be expressed from geometry as a function of the porosity fraction ϕ

$$D = \frac{180}{d_p^2} \frac{(1 - \phi)^2}{\phi^3}, \quad F = \frac{1.8}{d_p} \frac{1 - \phi}{\phi^3}, \quad (4)$$

where d_p is the particle (or Sauter mean) diameter [18, 19, 20, 21, 22].

2.2 2D study cases

To evaluate performance in mixed porous/fluid domains we designed several 2D benchmarks inspired by [13], replacing solid inclusions with porous ones (Fig. 1).

2.2.1 Manufactured solution test.

As verification step we used the *method of manufactured solutions* (MMS), prescribing artificial velocity/pressure fields and deriving forcing and boundary terms so that the pair is an exact solution. The dataset thus generated allows direct error evaluation of the PIPN framework. With added Darcy–Forchheimer terms, the forcing terms read

$$f_x = 2\mu u_x + \chi_p u_x (\mu D + \frac{1}{2} \rho F |\mathbf{u}|), \quad f_y = -2\mu u_y + \chi_p u_y (\mu D + \frac{1}{2} \rho F |\mathbf{u}|), \quad (5)$$

with $u_x = \cos(x) \sin(y)$, $u_y = -\cos(y) \sin(x)$. This provides a more demanding reference than the standard Navier–Stokes case.

2.2.2 Case studies.

Three classes of 2D experiments were considered:

- **Case 1:** baseline training using physics-informed and boundary losses only, with fixed D and F .
- **Case 2:** same geometries with different boundary conditions, simulating a porous object in an oil-filled duct. Parameters (viscosity, velocity, D , F) were chosen to yield stationary wake eddies. Data augmentation included shape scaling and rotations (Fig. 2).
- **Case 3:** variable inlet velocities, angles and porosity coefficients (D , F), with additional augmentations (translations, offsets, random perturbations) to test generalization to unseen shapes and conditions.

2.3 3D study cases

We extended to 3D domains inspired by windbreak studies [1]. Porous geometries representing tree canopies were generated from 3D models in Blender; convex hulls of single trees were arranged into rows, combined with house models [23] to increase complexity. Porosity was estimated from canopy images ($\phi = N_p/N$) and Darcy/Forchheimer coefficients computed via Eq. 4, using leaf length as d_p [24]. The tree species included were oak, pine, cypress, willow, acacia and eucalyptus. The kinematic viscosity was set to $14.61 \cdot 10^{-6} \text{ m}^2/\text{s}$ (air at 15°C), and inlet velocities ranged $[4 \cdot 10^{-6}, 10^{-5}] \text{ m/s}$, ensuring laminar regime. Randomization of tree sizes and positions produced sufficient variability (Fig. 3a–3b).

For all experiments, data were split into training/validation/test with 60/20/20 ratio.

3 Numerical Data Generation

3.1 CFD Simulations in OpenFOAM

Training data were generated with the open-source CFD toolbox *OpenFOAM*. Given the assumptions of steady, incompressible, laminar, Newtonian flow, we employed the `simpleFoam` solver [25], a finite-volume method based

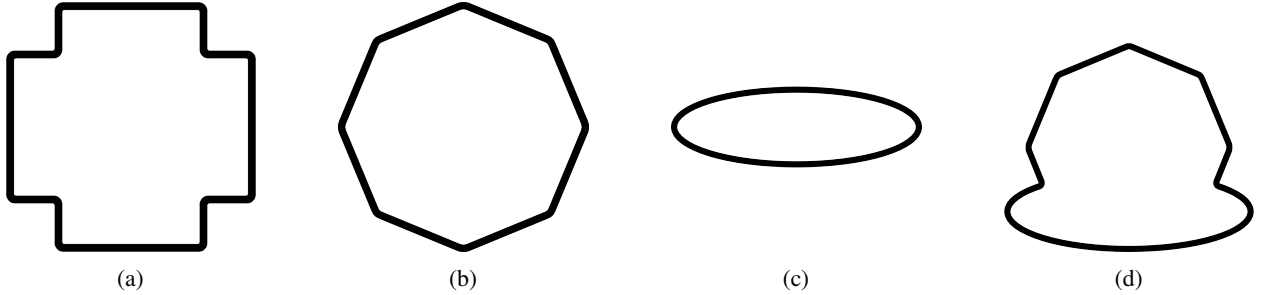


Figure 1: Some 2D porous geometries: (a–c) from training set, (d) unseen composite.

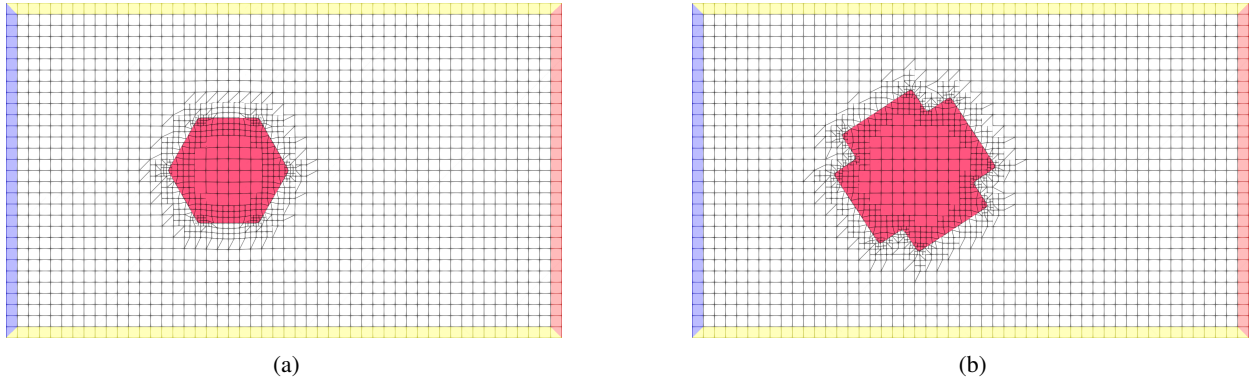


Figure 2: 2D domains generated with `snappyHexMesh`, boundary conditions: `inlet`, `outlet`, `wall`.

on the SIMPLE algorithm. Convergence thresholds were set to 10^{-4} and 10^{-3} for velocity and pressure, respectively. Mesh discretization was performed using the `snappyHexMesh` utility, starting from a base hexahedral grid and refining around porous obstacles and interfaces to improve accuracy. Examples of meshed domains are shown in Fig. 2. Boundary conditions in OpenFOAM were set as follows: velocity (fixedValue at inlet, inletOutlet at outlet, slip at walls) and pressure (zeroGradient at inlet/walls, fixedValue at outlet).

3.2 Point Cloud Representation

Since PointNet-based models require point clouds, OpenFOAM cell and face centers were converted into points annotated with velocity and pressure values. A binary flag identifies porous vs. free-fluid regions, with associated porosity coefficients. To ensure a fixed input size, the point clouds were uniformly sampled (preserving higher density near interfaces). Table 1 reports the sampling sizes for each experiment.

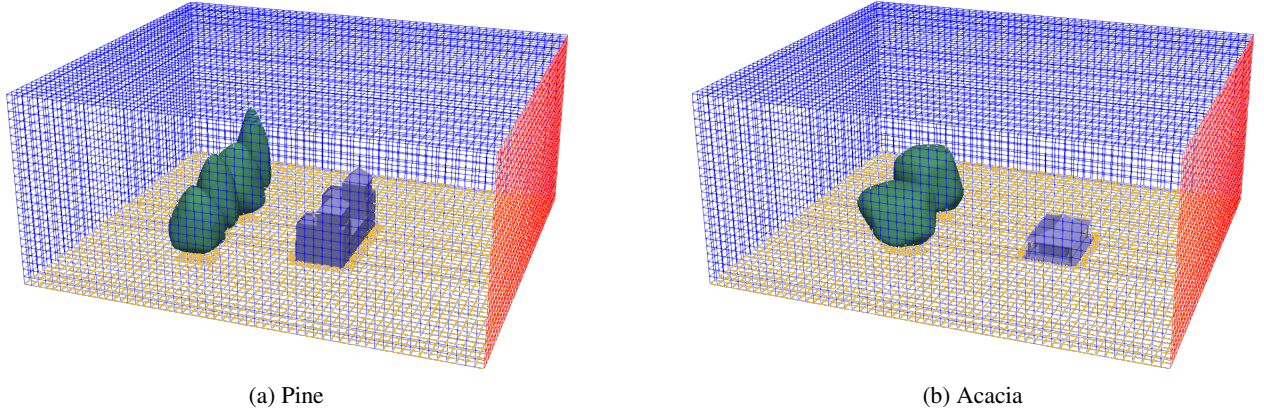


Figure 3: 3D domains with tree canopies, boundary conditions: `inlet`, `outlet`, `wall`.

Table 1: Training parameters of each experiment.

Experiment	λ_b	λ_m, λ_c	λ_d	α	Internal	Boundary	Observations
MMS	1	1	—	0.9995	667	168	—
Duct fixed, variable	1	1	100	0.9990	1000	200	500
Windbreak	1	10	1	0.9990	2000	1000	1000

Features were normalized: binary indices and porosity coefficients to $[0, 1]$, all other variables standardized with Z-score. Since the PDE residuals are computed on normalized values, the Navier–Stokes–Darcy equations were rescaled accordingly (cf. [26]). For example, Eq. 1 in 2D becomes

$$\frac{\sigma_{u_x}}{\sigma_x} \frac{\partial u_x}{\partial x} + \frac{\sigma_{u_y}}{\sigma_y} \frac{\partial u_y}{\partial y} = 0$$

with analogous scaling applied to the momentum equation. This ensures consistency between the standardized training data and the physics-informed loss.

4 Physics-Informed and Geometry-Aware ANNs

4.1 Physics-Informed Neural Networks

Physics-Informed Neural Networks (PINNs) solve PDEs by minimizing a loss function that combines agreement with available data and consistency with the governing equations. For the steady incompressible Navier–Stokes–Darcy equations (3) the PINN loss function takes the form:

$$\begin{aligned} \mathcal{L}(\theta) &= \lambda_m \mathcal{L}_m(\theta) + \lambda_c \mathcal{L}_c(\theta) + \lambda_b \mathcal{L}_b(\theta) + \lambda_d \mathcal{L}_d(\theta) \\ \mathcal{L}_c(\theta) &= \frac{1}{N_f} \sum_{i=1}^{N_f} \|\nabla \cdot \mathbf{u}_i^\theta\|^2 \\ \mathcal{L}_m(\theta) &= \frac{1}{N_f} \sum_{i=1}^{N_f} \left\| \rho (\mathbf{u}_i^\theta \cdot \nabla) \mathbf{u}_i^\theta + \nabla p_i^\theta - \mu \nabla^2 \mathbf{u}_i^\theta + \chi_{\Omega_p} \left(\mu D + \frac{1}{2} \rho F |\mathbf{u}_i^\theta| \right) \mathbf{u}_i^\theta \right\|^2 \\ \mathcal{L}_b(\theta) &= \frac{1}{N_b} \sum_{i=1}^{N_b} \|\mathbf{u}_i^\theta - \mathbf{u}_i\|^2 + \|p_i^\theta - p_i\|^2 \quad \mathcal{L}_d(\theta) = \frac{1}{N_d} \sum_{i=1}^{N_d} \|\mathbf{u}_i^\theta - \mathbf{u}_i\|^2 + \|p_i^\theta - p_i\|^2 \end{aligned}$$

Here: N_d is the number of data points where measurements or simulation data are available; N_f is the number of collocation points used to enforce the PDE; N_b, N_f is the number of collocation points used to enforce the boundary conditions and equations respectively; θ are the network parameters. χ_{Ω_p} is 1 if the collocation point is inside the porous domain, 0 otherwise. This formulation allows to remove the porous term in the fluid region. $\lambda_d, \lambda_f, \lambda_b$ are parameters which controls the importance of each loss term. \mathcal{L}_d ensures agreement with available data; $\mathcal{L}_c, \mathcal{L}_m$ penalize violations of the governing equations using automatic differentiation to compute derivatives; \mathcal{L}_b term enforces that the boundary conditions. Automatic differentiation is a technique for evaluating exact derivatives of a computational graph by systematically applying the chain rule, allowing gradients of PDE residuals to be obtained with machine precision and without symbolic derivation.

4.2 Physics-informed PointNets

A key point is that a PINN is trained on a single geometry and cannot directly generalize to new shapes: this requires retraining for each case. Such limitation makes conventional PINNs impractical for exploring a wide range of geometric configurations in industrial design.

Physics-Informed PointNets (PIPNs) extend this concept to unstructured geometric domains by combining the PINN framework with the PointNet architecture, which processes 3D or 2D point clouds in a permutation-invariant way.

In PIPN, the input is a point cloud representing both the geometry and the associated physical coordinates, and the network outputs the predicted fields. The physics-informed loss is then applied to these outputs at the point level, enabling the model to generalize across different domain shapes without remeshing or reparameterization.

Compared to the original PIPN formulation, our implementation incorporates porous-media-specific terms in the PDE residuals, allowing the same framework to handle both Navier–Stokes and Darcy-modified equations within their respective subdomains. Furthermore, the approach is extended to fully 3D problems, requiring modifications in the PointNet architecture and the derivative computation pipeline to handle 3D spatial gradients efficiently.

4.2.1 Architecture

The first step of this work was to extend the existing PIPN architecture [13] to take into account the porous medium. This proposed model is based on PointNets[12] but adds the physics loss to the training process. This involved two main challenges: the porous zone had to be input to the model and the losses had to be modified to disable the source term if the collocation point was not porous. Therefore the final implementation added a Signed Distance Function (SDF) to the input points and a binary indicator feature ID to the momentum losses, corresponding to χ_{Ω_p} in $\mathcal{L}_{\mathbb{P}}$. This allows the source term to be disabled if a collocation point is inside the fluid region and at the same time ensures the correctness of the automated differentiation process. Figure 4a shows a diagram of such architecture with the associated input dimension of each layer. As opposed to the original PIPN implementation the input included the position of each point $X \in R^d$ the SDF function associated to the point and a one hot encoded feature representing the type of boundary condition (Id_b). To improve the the global embedding the SDF and boundary id were concatenated to the output of the first shared layers which is then used to generate the global embedding representation of the domain. This allows the global embedding to incorporate both positional information and porosity information. The rest of the architecture is the same as the original PIPN implementation.

4.3 Physics-Informed Geometry-Aware Neural Operator

While PIPN processes each geometry as an independent point cloud and learns a mapping from coordinates and physical parameters to flow fields, it still operates on fixed boundary conditions on all samples.

PI-GANO [14] extends this concept by embedding both the geometry and variable boundary conditions into a neural operator framework, which learns a mapping between parametrized function spaces. This is achieved by representing the geometry in a latent space and the boundary conditions into another latent space. The two representations, together with the permutation invariant representation of each point are then combined to predict the behavior of the physical system.

4.3.1 Architecture

The model was implemented as per the original paper but the porous SDF and Id_b features were added to the Geometry Encoding module. Moreover the sum operation before the output was replaced with a shared MLP layer. This last modification has the advantage of not using multiple branches for each variable, therefore reducing the number of operations and parameters while obtaining better performance. The variable inlet velocity U and the Darcy and Forchheimer coefficients (D and F) were added as inputs to the branch module together with the positions at which the boundary condition was available. If one of the conditions was not available at that position, its value was set to 0. Finally the ID feature was added to the momentum losses as in the PIPN. To take advantage of the mini-batching mechanism the number of points M input to the branch was fixed, using the ratio of the minimum number of points of each boundary to the number of total boundary samples.

4.4 Training

All the models were trained using the SiLU [27] activation function while in the manufactured solutions experiment the hyperbolic tangent was used. In all experiments the Adam optimizer with a learning rate of 0.001 and an exponential learning rate decay α was used. In all experiments but the manufactured solutions one a dropout layer with $p = 0.05$ was added to the last two layers before the output to prevent overfitting. All model were trained for 3000 epochs to allow convergence and the loss coefficients were set according to Table 1. Those values allowed to obtain accurate results and were set through experimentation on different cases. It must be noted that the final values are consistent with [28].

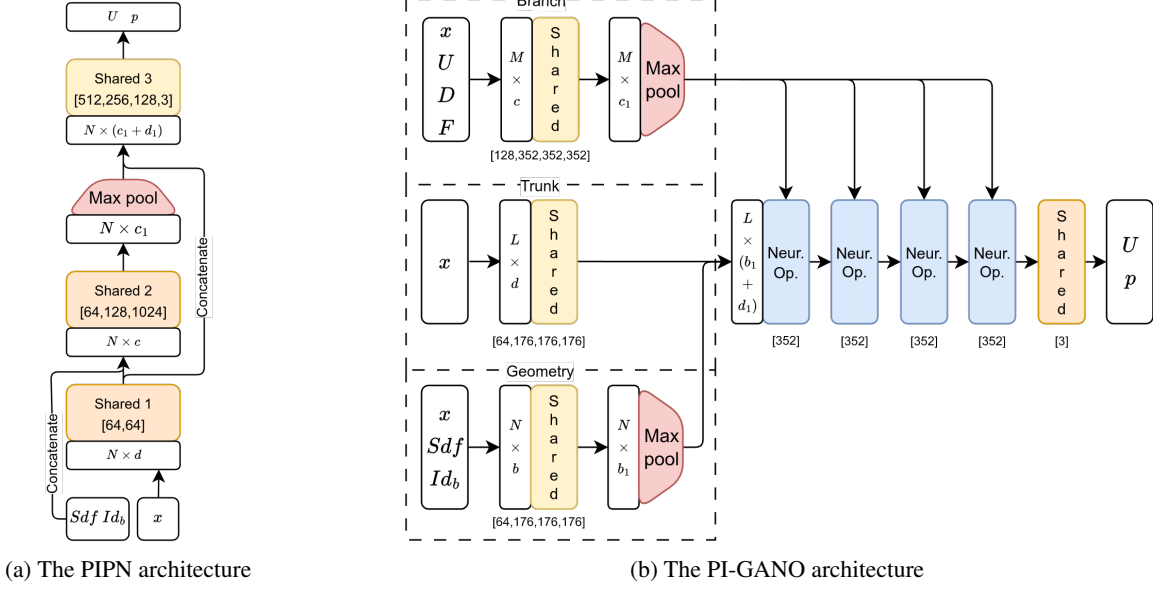


Figure 4: Architectures modified to take into account porous medium.

Training			Unseen		
Global	Porous region	Fluid region	Global	Porous region	Fluid region
u_x	$1.20 \cdot 10^{-2}$	$1.20 \cdot 10^{-2}$	$1.20 \cdot 10^{-2}$	$1.23 \cdot 10^{-2}$	$1.23 \cdot 10^{-2}$
u_y	$9.39 \cdot 10^{-3}$	$8.13 \cdot 10^{-3}$	$9.63 \cdot 10^{-3}$	$9.38 \cdot 10^{-3}$	$8.14 \cdot 10^{-3}$
p	$1 \cdot 10^{-2}$	$8.93 \cdot 10^{-3}$	$1.02 \cdot 10^{-2}$	$1.02 \cdot 10^{-2}$	$8.73 \cdot 10^{-3}$

Table 2: MMS errors of the PIPN predictions.

5 Experimental Results

5.1 Case 1: Manufactured solutions

We use the PIPN of Fig. 4a. Performance, reported as MAE, is comparable to [13] on both training and unseen geometries (Table 2).

Errors are uniformly low; the porous subdomain tends to be slightly easier than the free-flow region. Fig. 5 (unseen sample) shows no structured error bias.

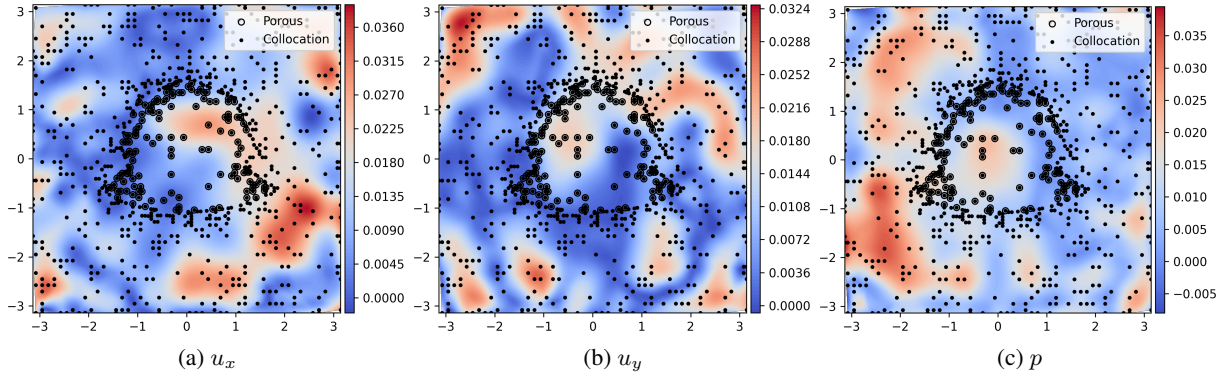


Figure 5: MAE obtained from the PIPN prediction on the unseen geometry in Fig. 1.

	Test			Unseen		
	Global	Porous region	Fluid region	Global	Porous region	Fluid region
u_x	$3.1 \cdot 10^{-3}$	$3.6 \cdot 10^{-3}$	$3.1 \cdot 10^{-3}$	$9.3 \cdot 10^{-3}$	$1.1 \cdot 10^{-2}$	$9.1 \cdot 10^{-3}$
u_y	$1.2 \cdot 10^{-3}$	$2.1 \cdot 10^{-3}$	$1.1 \cdot 10^{-3}$	$3.7 \cdot 10^{-3}$	$6.2 \cdot 10^{-3}$	$3.4 \cdot 10^{-3}$
p	$9 \cdot 10^{-4}$	$1.7 \cdot 10^{-3}$	$8 \cdot 10^{-4}$	$6.5 \cdot 10^{-3}$	$8.8 \cdot 10^{-3}$	$6.2 \cdot 10^{-3}$

Table 3: MAE of the PIPN predictions with fixed boundary conditions.

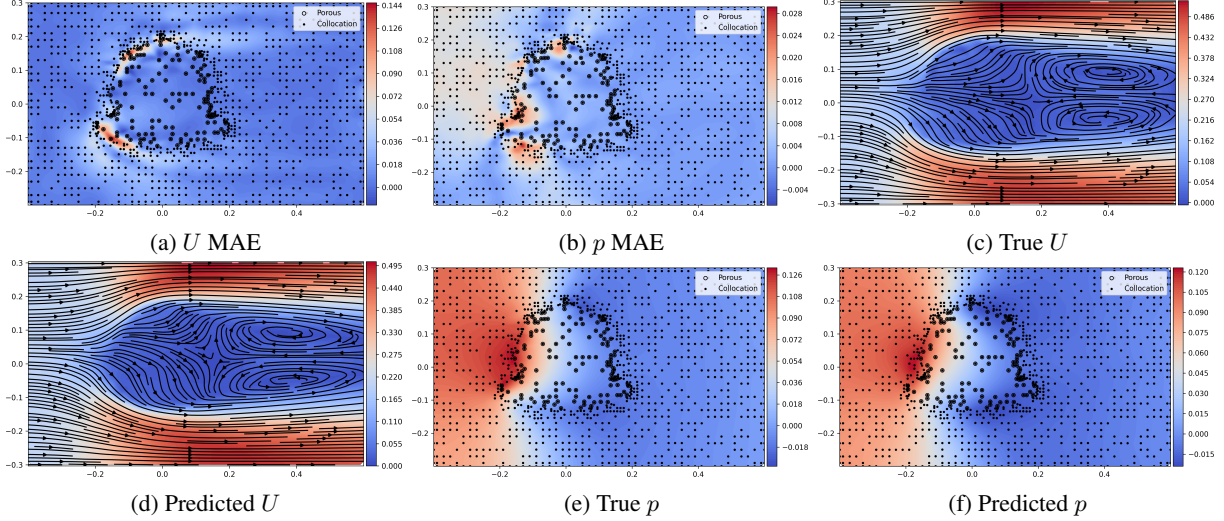


Figure 6: Errors, prediction and ground truth on an unseen 2D geometry (cf. Fig. 1).

5.2 Case 2: 2D porous flow with fixed boundary conditions

We reuse the PIPN as above. Table 3 reports MAE on test and unseen sets.

Errors remain low; u_x is consistently the most challenging (stronger gradients across the porous/free-flow interface). Errors are higher on the unseen set. Fig. 6 (unseen geometry) illustrates error localization near sharp corners and correct wake prediction. The average simulation time on the test set is 0.02s while OpenFOAM took 1.17s, providing a significant speedup.

5.3 Case 3: 2D porous flow with variable boundary conditions

We evaluate PI-GANO (larger geometry embedding; cf. Fig. 4b) on test and unseen sets with BCs/parameters beyond training ranges.

As expected, errors increase on unseen BCs yet remain acceptable; u_x is again the most sensitive. Fig. 7 shows a challenging unseen case (high porosity; obstacle nearly spanning the duct width), with underprediction in high-gradient regions but correct wake reconstruction. Grouping unseen errors by Darcy coefficient (Table 5) shows pressure MAE

	Test			Unseen		
	Global	Porous region	Fluid region	Global	Porous region	Fluid region
u_x	$1.95 \cdot 10^{-3}$	$1.63 \cdot 10^{-3}$	$1.99 \cdot 10^{-3}$	$1.57 \cdot 10^{-2}$	$1.90 \cdot 10^{-2}$	$1.53 \cdot 10^{-2}$
u_y	$8.47 \cdot 10^{-4}$	$9.05 \cdot 10^{-4}$	$8.40 \cdot 10^{-4}$	$5.12 \cdot 10^{-3}$	$5.25 \cdot 10^{-3}$	$5.10 \cdot 10^{-3}$
p	$4.00 \cdot 10^{-4}$	$6.43 \cdot 10^{-4}$	$4.77 \cdot 10^{-4}$	$6.86 \cdot 10^{-3}$	$7.35 \cdot 10^{-3}$	$6.80 \cdot 10^{-3}$

Table 4: MAE of the PI-GANO predictions with variable boundary conditions.

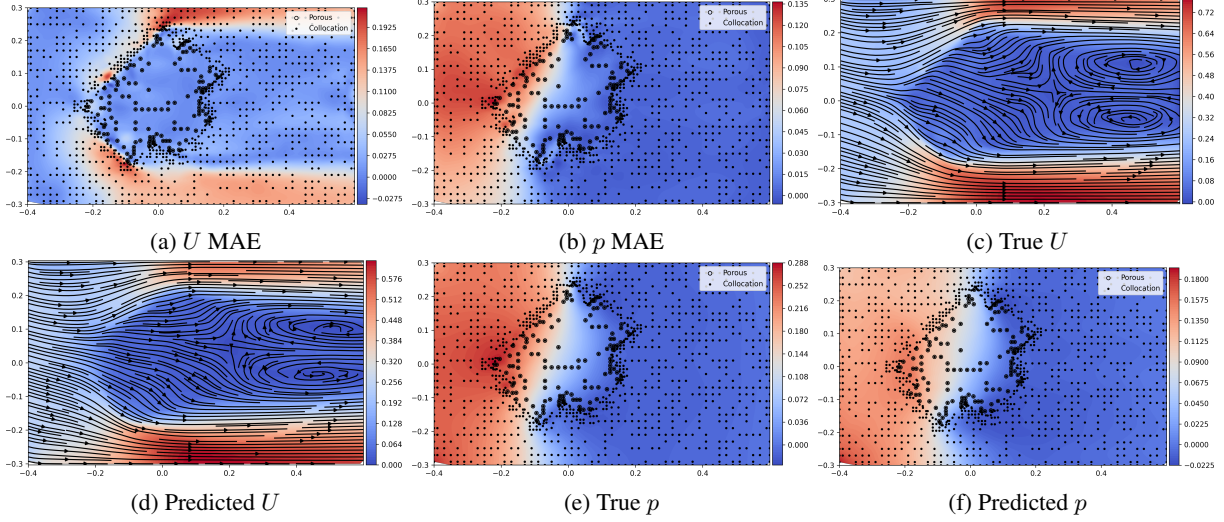


Figure 7: Errors, prediction and ground truth on an unseen geometry ($D=1.4 \cdot 10^4$, $u_x=0.257$ m/s, angle -15.83°).

D	1000	2000	14000	16000
u_x	$2.77 \cdot 10^{-2}$	$1.85 \cdot 10^{-2}$	$2.36 \cdot 10^{-2}$	$4.16 \cdot 10^{-2}$
u_y	$6.96 \cdot 10^{-3}$	$6.94 \cdot 10^{-3}$	$1.11 \cdot 10^{-2}$	$1.38 \cdot 10^{-2}$
p	$4.79 \cdot 10^{-3}$	$1.40 \cdot 10^{-2}$	$2.11 \cdot 10^{-2}$	$4.49 \cdot 10^{-2}$

Table 5: Unseen D average MAE errors.

increasing with D , while velocity MAE varies modestly. The average simulation time on the test set is 0.01s while OpenFOAM took 2.08s.

5.4 Case 4: 3D porous flow

We test PI-GANO in 3D (512-dimensional latent geometry space; 16-bit mixed precision). Besides fluid and porous regions, MAE is also reported on solid surfaces to probe boundary fidelity (Table 6).

Largest errors occur for u_x and inside tree canopies (complex geometry and high gradients). Still, accuracy is satisfactory given the geometric complexity. Fig. 8 shows streamlines and surface errors for the worst u_x case (eucalyptus canopy; tapered shape yields stronger impact on the house and complex mixing). The model captures wakes and recirculations; errors concentrate where low-speed wakes interact with free stream. The average simulation time on the test set is 0.014s while OpenFOAM took 20.04s per case.

	Global	Fluid region	Porous region	Solid surface
u_x	$1.15 \cdot 10^{-7}$	$1.14 \cdot 10^{-7}$	$1.34 \cdot 10^{-7}$	$8.86 \cdot 10^{-8}$
u_y	$4.14 \cdot 10^{-8}$	$4.12 \cdot 10^{-8}$	$4.44 \cdot 10^{-8}$	$3.89 \cdot 10^{-8}$
u_z	$3.18 \cdot 10^{-8}$	$3.10 \cdot 10^{-8}$	$4.80 \cdot 10^{-8}$	$2.65 \cdot 10^{-8}$
p	$2.39 \cdot 10^{-12}$	$2.15 \cdot 10^{-12}$	$6.96 \cdot 10^{-12}$	$3.52 \cdot 10^{-12}$

Table 6: MAE of the PI-GANO predictions on the windbreaks test set.

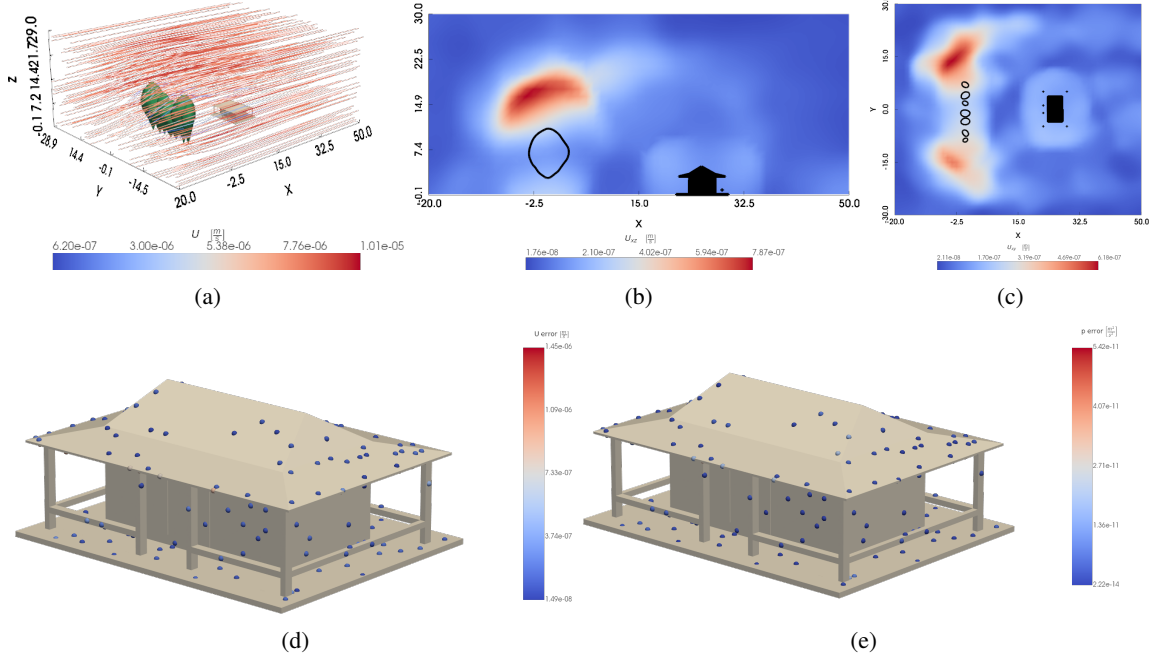


Figure 8: Predicted U streamlines (a), sliced xz/xy U errors (b,c), and surface errors on the house for U and p (d,e).

6 Discussion and Conclusions

The proposed methodology allows to effectively model the behavior of mixed fluid-porous medium using PINNs. The tests confirm the ability of the models to generalize not only with respect to variable domain geometries, but also to boundary conditions and material porosity levels.

The experiments prove the effectiveness of the approach in both 2D and more complex 3D cases. Moreover the models were able to predict the flow over a mix of solid and porous materials. Predictions on unseen geometries and boundary conditions show acceptable errors even on cases with configurations not found in the training set.

However, the models proved to have difficulties in obtaining accurate results on flow fields with steep gradients, especially on u_x . Several approaches are viable to solve this problem. The first one is the replacement of the geometry encoding block with a PointNet++ based one. This could improve the latent representation of the domain by exploiting the hierarchical architecture proposed in [29]. Another strategy could be to use an architecture based on Fourier Neural Operators [30, 31]. However judging by the experiment carried out in [30], the model could potentially need a larger number of parameters with respect to the PointNet-based implementations with a consequent increase in training times.

To lift the constraint of low velocities and laminar flow assumptions, it would be necessary to move to a model which takes into account the turbulence of the flow, such as the Reynolds Averaged Navier Stokes equations together with a turbulence closure model such as the $k - \epsilon$ model [32]. This would however require to add new terms to the loss, therefore making the optimization problem more difficult, especially with respect to the setting of the scaling parameters. Even if automatic methods have been proposed [33, 34] to balance the loss terms, they are not guaranteed to work on each specific case.

Finally, a sampling strategy could be implemented that takes into account the problematic areas of each experiment, potentially leading to an increase in precision inside those regions.

Acknowledgments

Computational resources provided by hpc-ReGAInS@DISCo. The work was also partially supported by the European Union’s Horizon 2020 Research and Innovation Programme under the CISC project (Marie Skłodowska-Curie grant agreement no. 955901); by the MUSA-Multilayered Urban Sustainability Action project, funded by the European Union-NextGenerationEU, (CUP G43C22001370007, Code ECS00000037); by Project ReGAInS (code 2023-NAZ-0207/DIP-ECC-DISCO23), funded by the Italian University and Research Ministry, within the Excellence Departments program

2023-2027 (law 232/2016); and by the project FAIR - Future AI Research-Spoke 4-PE00000013 D53C22002380006, funded by the European Union-Next Generation EU within the project NRPP M4C2, Investment 1.,3 DD. 341.

References

- [1] Ahmed Osama Mahgoub and Saud Ghani. Numerical and experimental investigation of utilizing the porous media model for windbreaks cfd simulation. *Sustainable Cities and Society*, 65:102648, 2021.
- [2] Sergio Caucao, Marco Discacciati, Gabriel N Gatica, and Ricardo Oyarzúa. A conforming mixed finite element method for the navier–stokes/darcy–forchheimer coupled problem. *ESAIM: Mathematical Modelling and Numerical Analysis*, 54(5):1689–1723, 2020.
- [3] Flavio Cimolin and Marco Discacciati. Navier–stokes/forchheimer models for filtration through porous media. *Applied Numerical Mathematics*, 72:205–224, 2013.
- [4] Umurdin Dalabaev and Nusratilla Latipov. Currents with underwater porous obstacles. In *E3S Web of Conferences*, volume 542, page 06004. EDP Sciences, 2024.
- [5] Mehdi Dehghan and Zeinab Gharibi. A fully mixed virtual element method for darcy–forchheimer miscible displacement of incompressible fluids appearing in porous media. *IMA Journal of Numerical Analysis*, 44(2):797–835, 2024.
- [6] Antonios Parasyris, Christopher Brady, Diganta Bhusan Das, and Marco Discacciati. Computational modeling of coupled free and porous media flow for membrane-based filtration systems: A review. *Journal of Applied Membrane Science & Technology*, 23(3), 2019.
- [7] Iryna Rybak, Christoph Schwarzmeier, Elissa Eggenweiler, and Ulrich Rüde. Validation and calibration of coupled porous-medium and free-flow problems using pore-scale resolved models. *Computational Geosciences*, 25(2):621–635, 2021.
- [8] Giuseppe A Zampogna and Alessandro Bottaro. Fluid flow over and through a regular bundle of rigid fibres. *Journal of Fluid Mechanics*, 792:5–35, 2016.
- [9] J.F. Wendt. *Computational Fluid Dynamics: An Introduction*. Springer, 2008.
- [10] Kathleen R Dupre. *Relating porous media structure to the Darcy-Forchheimer model*. PhD thesis, Boston University, 2020.
- [11] M. Raissi, P. Perdikaris, and G.E. Karniadakis. Physics-informed neural networks: A deep learning framework for solving forward and inverse problems involving nonlinear partial differential equations. *J. of Comp. Physics*, 378:686–707, 2019.
- [12] Charles R. Qi, Hao Su, Kaichun Mo, and Leonidas J. Guibas. Pointnet: Deep learning on point sets for 3d classification and segmentation. In *Proc.s IEEE Conf. on Computer Vision and Pattern Recognition (CVPR)*, pages 652–660, 2017.
- [13] Ali Kashefi and Tapan Mukerji. Physics-informed pointnet: A deep learning solver for steady-state incompressible flows and thermal fields on multiple sets of irregular geometries. *Journal of Computational Physics*, 468:111510, 2022.
- [14] W. Zhong and H. Meidani. Physics-informed geometry-aware neural operator. *Computer Methods in Applied Mechanics and Engineering*, 2025.
- [15] H. Jasak. Openfoam: Open source cfd in research and industry. *International Journal of Naval Architecture and Ocean Engineering*, 1(2):89–94, 2009.
- [16] Ciceri L. Gallinatore/porous-cfd: Medes25. <https://doi.org/10.5281/zenodo.18450116>, February 2026.
- [17] Malay K Das, Partha P Mukherjee, and Kambadur Muralidhar. Equations governing flow and transport in porous media. In *Modeling transport phenomena in porous media with applications*, pages 15–63. Springer, 2017.
- [18] J. Kozeny. Über kapillare leitung des wassers im boden. *Sitzungsber. Akad. Wiss. Wien*, 136:271–306, 1927.
- [19] P. C. Carman. Fluid flow through granular beds. *Transactions of the Institution of Chemical Engineers*, 15:150–166, 1937.
- [20] P. C. Carman. *Flow of Gases Through Porous Media*. Butterworths Scientific Publications, London, 1956.
- [21] Maasoud Kaviani. *Principles of heat transfer in porous media*. Springer Science & Business Media, 2012.
- [22] Kambiz Vafai. *Handbook of porous media*. CRC Press, 2015.

[23] Daryl Peralta, Joel Casimiro, Aldrin Michael Nilles, Justine Aletta Aguilar, Rowel Atienza, and Rhandley Cajote. Next-best view policy for 3d reconstruction. *arXiv preprint arXiv:2008.12664*, 2020.

[24] Forest Ecology and Forest Management Group. Tree database. <https://www.wur.nl/en/research-results/chair-groups/environmental-sciences/forest-ecology-and-forest-management-group/education/tree-database.htm>, 2025. Wageningen University & Research; educational resource on tree species autecology.

[25] L. S. Caretto, A. D. Gosman, S. V. Patankar, and D. B. Spalding. Two calculation procedures for steady, three-dimensional flows with recirculation. In Henri Cabannes and Roger Temam, editors, *Proceedings of the Third International Conference on Numerical Methods in Fluid Mechanics*, pages 60–68. Springer Berlin Heidelberg, 1973.

[26] Shengfeng Xu, Yuanjun Dai, Chang Yan, Zhenxu Sun, Renfang Huang, Dilong Guo, and Guowei Yang. On the preprocessing of physics-informed neural networks: How to better utilize data in fluid mechanics. *Journal of Computational Physics*, 528:113837, 2025.

[27] Stefan Elfwing, Eiji Uchibe, and Kenji Doya. Sigmoid-weighted linear units for neural network function approximation in reinforcement learning. *Neural networks*, 107:3–11, 2018.

[28] Jan Hauke Harmening, Fabian Pioch, Lennart Fuhrig, Franz-Josef Peitzmann, Dieter Schramm, and Ould el Moctar. Data-assisted training of a physics-informed neural network to predict the separated reynolds-averaged turbulent flow field around an airfoil under variable angles of attack. *Neural Computing and Applications*, 36(25):15353–15371, 2024.

[29] Charles Ruizhongtai Qi, Li Yi, Hao Su, and Leonidas J Guibas. Pointnet++: Deep hierarchical feature learning on point sets in a metric space. *Advances in neural information processing systems*, 30, 2017.

[30] Zongyi Li, Nikola Kovachki, Chris Choy, Boyi Li, Jean Kossaifi, Shourya Otta, Mohammad Amin Nabian, Maximilian Stadler, Christian Hundt, Kamyar Azizzadenesheli, et al. Geometry-informed neural operator for large-scale 3d pdes. *Advances in Neural Inform. Proc. Sys.*, 36:35836–35854, 2023.

[31] Colin White, Julius Berner, Jean Kossaifi, Mogab Elleithy, David Pitt, Daniel Leibovici, Zongyi Li, Kamyar Azizzadenesheli, and Anima Anandkumar. Physics-informed neural operators with exact differentiation on arbitrary geometries. In *The symbiosis of deep learning and differential equations III*, 2023.

[32] B.E. Launder and D.B. Spalding. The numerical computation of turbulent flows. *Computer Methods in Applied Mechanics and Engineering*, 3(2):269–289, 1974.

[33] Qiang Liu, Mengyu Chu, and Nils Thuerey. Config: Towards conflict-free training of physics informed neural networks. *arXiv preprint arXiv:2408.11104*, 2024.

[34] Rafael Bischof and Michael A. Kraus. Multi-objective loss balancing for physics-informed deep learning. *Computer Meth. in Appl. Mechanics and Engineering*, 439:117914, 2025.